

Design and mechanical analysis of the PRAGYA tokamak vacuum vessel

Ravi Gupta^a, Rahul Babu Koneru^a, Saptarshi Rajan Sarkar^a, Santosh Ansumali^b, Animesh Kuley^c, Roshan George^a, Shaurya Kaushal^{a,*}

^a*Pranos Fusion Private Limited, Innovation and Development Centre, JNCASR, Bengaluru, Karnataka, 562162, India*

^b*Engineering Mechanics Unit, Jawaharlal Nehru Centre for Advanced Scientific Research, Bengaluru, 560064, India*

^c*Department of Physics, Indian Institute of Science, Bangalore, 560012, India*

Abstract

PRAGYA is a new and India's first privately developed low aspect ratio tokamak device designed by Pranos Fusion Energy. The tokamak is designed for a plasma major radius (R_0) of about 0.4 m, plasma minor radius (a) greater than 0.18 m, plasma current (I_p) of up to 25 kA and a toroidal magnetic field (B_T) of 0.1 T. The PRAGYA vacuum vessel has distinctive features such as a toroidal electric break to minimize induced eddy current and a double O-ring arrangement to minimize the loss of vacuum. This paper details the final design of the PRAGYA vacuum vessel and presents a comprehensive three-dimensional (3D) finite element model (FEM) assessment of its structural performance. Evaluations cover the effects of self-weight, atmospheric load and thermal stress arising from in-situ baking. The results confirm that the design satisfies all required safety margins under these combined loading conditions, providing a robust foundation for subsequent plasma operations in this compact tokamak.

Keywords:

1. Introduction

An ever-increasing global energy demand, largely met by fossil fuels, is accelerating anthropogenic climate change. Robust low carbon energy alternatives

*shaurya@pranosfusion.energy

are essential to reduce greenhouse gas emissions and nuclear fusion offers a safe and energy dense alternative to the existing set of green energy technologies. Magnetic-confinement fusion (MCF), with the tokamak as its most extensively studied and experimentally validated configuration, aims to satisfy the Lawson energy-balance requirement by confining a 10 keV plasma long enough that alpha self-heating together with auxiliary heating exceeds losses due to transport and radiation (Lawson, 1957; ITER Physics Expert Group on Confinement and Transport and ITER Physics Expert Group on Confinement Modelling and Database and ITER Physics Basis Editors, 1999). The current barriers to tokamaks as commercial power sources are primarily around achieving high energy confinement despite microturbulence driven anomalous transport (Horton, 1999); maintaining stable operation against MHD instabilities and disruptions while controlling current and pressure profiles (Hender et al., 2007); and realizing a durable plasma–material interface that can simultaneously handle extreme steady state and transient heat fluxes and provide reliable power and particle exhaust (divertor/first-wall performance) (Federici et al., 2001; Herrmann, 2002).

Against this multi-constraint background, decades of research has produced major advances in both tokamak physics and the enabling technologies. The record fusion gain and triple product by JET (Keilhacker, 1999), TFTR (Strachan et al., 1997) and JT-60U (Kishimoto et al., 2005), discovery of the new operational regime H-mode by ASDEX-U (Wagner et al., 1982), development of spherical tokamaks such as MAST (Darke et al., 1995), NSTX (Ono et al., 2001), allowing for a high plasma β (β =plasma pressure/magnetic pressure) operations in a compact space. In parallel, state-of-the-art high-temperature superconducting (HTS) rare earth barium copper oxide (REBCO) magnets have demonstrated large-scale, ~ 20 T-class fields, strengthening the case for compact high-field tokamak concepts (Hartwig et al., 2023; Whyte et al., 2023). High-performance computing and integrated predictive modelling frameworks increasingly couple microturbulence, transport, pedestal and equilibrium physics, MHD stability and engineering constraints, enabling a more constrained scenario development and design iteration (Staebler et al., 2022; Lyons et al., 2023; Jenko, 2025). Novel plasma control systems based on machine learning are being actively developed for improved flexibility and generalizability (Degraeve et al., 2022; Kerboua-Benlarbi et al., 2024). With ITER and SPARC progressing towards first plasma operations, the field is now positioned to test fusion net-gain relevant regimes with substantially improved physics understanding and technology readiness.

A central design variable in tokamaks is the aspect ratio A , which strongly couples to MHD stability limits and engineering integration. The aspect ratio is

defined as the ratio of plasma major radius R_0 to the plasma minor radius a . A schematic of the plasma geometry is shown in Figure 1. From a magneto-

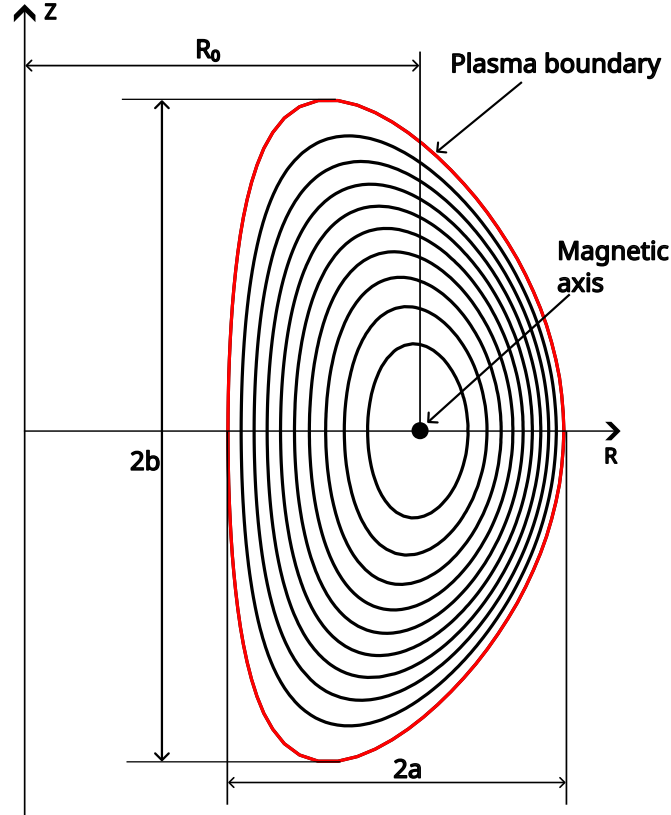


Figure 1: A schematic of the plasma geometry depicting the magnetic contours inside the last closed flux surface (LCFS) which is shown in red. The plasma major radius R_0 is defined as the radial distance from the axis of rotation to the plasma magnetic axis. The plasma minor radius $a = (R_{max} - R_{min})/2$ where R_{max} and R_{min} are the maximum and the minimum radial extents of the LCFS respectively. The ellipticity $\kappa = b/a$ and triangularity $\delta = (R_{geo} - R_{up/low})/a$ where R_{geo} is the geometric center of the plasma and $R_{up/low}$ is the radial extent of the uppermost or the lowermost point on the LCFS.

dynamic (MHD) stability point of view, a higher plasma β offers better stability against ballooning and kink modes. As the plasma β scales as $1/A$, a smaller A is favoured for stable operations (Miller et al., 1996). At one end are the ultra-compact spherical tokamaks (STs) such as PEGASUS-III (Sontag et al., 2022),

MAST (Darke et al., 1995), NSTX (Ono et al., 2001), SUNIST (Ying et al., 2003), LATE (Maekawa et al., 2005), LTX- β (Boyle et al., 2023; Banerjee et al., 2024) with $A < 2$. These machines allow for operations at a high β , a high plasma current and a high bootstrap fraction (Peng, 2000; Ono and Kaita, 2015). However, the lack of space at the high-field side poses a challenge to placing a central solenoid, shielding and blankets. On the other end of the aspect ratio spectrum are EAST ($A = 4.25$) (Wu et al., 2007), SST-1 ($A = 5.5$) (Deshpande, 1997), WEST ($A > 5.6$) (Bucalossi et al., 2022) which are not constrained for space but are prone to MHD instabilities. The remainder of the aspect ratio range has tokamaks such as DIII-D ($A = 2.5$) (Luxon, 2002), JT-60SA ($A = 2.5$) (Tomarchio et al., 2017), ADITYA ($A = 3.0$) (Bhatt et al., 1989), Alcator C-Mod ($A = 3.09$) (Marmor and Group, 2007), SPARC ($A = 3.24$) (Creely et al., 2020), KSTAR ($A = 3.6$) (Lee et al., 2001) which offer exploration of various physics and subsystems for ITER and DEMO-like machines (Tomarchio et al., 2017). Wong and co-authors (Wong et al., 2002) in their analysis observed that for an elongation of 2, the minimum cost of electricity was obtained for $A \in [2, 3]$ and $A \sim 2$ for a superconducting (SC) reactor and a normal conducting (NC) reactor respectively. The analysis explored the combined effect of aspect ratio (1.2 – 6.0), elongation (1.5, 3.0) and MHD stability on the design of NC and SC fusion reactors. From an economics standpoint, along with the trade-off between available space inside a tokamak and MHD stability, the low aspect ratio tokamaks are very promising in the context of a pilot fusion power plant.

Within this landscape, PRAGYA is being developed as India’s first privately developed low aspect ratio tokamak designed by Pranos Fusion Energy. PRAGYA is designed for a plasma major radius R_0 of 0.4 m and minor radius a of 0.18 m which gives $A \sim 2.2$ with a planned operational plasma current I_p of about 25 kA. The magnetic system consists of a central solenoid along with the toroidal and poloidal field coils. The toroidal field coils are designed to produce a magnetic field B_T of strength 0.1 T at R_0 . The plasma current will be driven by a central solenoid while a 6 kW microwave source operating at 2.45 GHz will be used for pre-ionization and plasma startup. The target vacuum pressure is 10^{-6} mbar. This is a small compact tokamak designed as a precursor to a larger tokamak with scientific exploration and development of critical human resources as a core objective. In particular, PRAGYA is designed to address the following objectives:

- i. accommodate plasma with an elongation between 1.5 and 2.2 and a triangularity between 0.0 and 0.4
- ii. test bed for superconductor magnets, auxiliary heating, solenoid-free start-up

- and current drive, novel plasma control systems for future large-scale fusion device
- iii. investigate the magnetohydrodynamic (MHD) stability of plasma
 - iv. test remote handling.

The vacuum vessel is a crucial component of tokamak maintaining a very high vacuum necessary for plasma generation, confinement and shaping. In addition to the vacuum load and the self-weight, the vacuum vessel is also subjected to thermal load during baking operations, electromagnetic loads from the magnetic system and also large asymmetric loads encountered during plasma disruption events. Additionally, a vacuum vessel provides support for plasma facing components such as limiters and divertors along with diagnostics such as flux loops and Rogowski coils. Furthermore, the vacuum vessel also acts as a support structure for the toroidal field (TF) and the poloidal field (PF) coils. The design of the vessel should ensure requisite level of vacuum pressure and structural integrity against the aforementioned loads all the while sparing enough room for diagnostics.

The primary focus of this paper is the design of PRAGYA tokamak's vacuum vessel. The vessel is designed to strictly adhere to the safe structural and thermal loads encountered during the tokamak operation. Detailed simulations are conducted to assess the structural integrity of vacuum vessel. The remainder of the paper is organized as follows. The mechanical design of the vacuum vessel and a detailed description of its various components are presented in Section 2. The results from the thermo-mechanical stress analysis are discussed in Section 3 wherein results from 3D FEA analysis of mechanical and thermal loads on the vacuum vessel are discussed. Finally, the conclusions are drawn and a future outlook of PRAGYA is provided in Section 4

2. Mechanical design of the vacuum vessel

2.1. Description of the vacuum vessel

PRAGYA tokamak is being designed for a plasma major radius of 0.4 m, a plasma minor radius of 0.13 m - 0.18 m and a plasma current of upto 25 kA. The resulting aspect ratio is between 2.2 and 3.1. The key target operational parameters of PRAGYA are listed in Table 1. The bounds of the operational limits are subject to safety factor on axis q_0 and on the edge q_{95} that allow for a stable plasma operation. For a given geometry of the plasma, q_0 and q_{95} are computed using the fixed-boundary Grad-Shafranov solver in TokaMaker (Hansen et al., 2024). These values are listed for the minimum and maximum values of A and δ in Table

2. A short description of the Grad-Shafranov equation is provided in Appendix C. Based on the aforementioned requirements and budgetary constraints, a vacuum vessel of width 400 mm and a height of 600 mm is designed. The wall thickness of the vacuum vessel is 6 mm on all sides. This particular choice of the wall thickness was result of an optimization procedure set to minimize the maximum stress on the vessel and is discussed in Section 3. The resulting inner diameter (ID) and the outer diameter (OD) of the vessel are 388 mm and 1212 mm respectively with a total interior volume of 0.8 m^3 . The 3D computer aided design (CAD) model of the vacuum vessel assembly is shown in Figure 2. To provide electrical insulation, the vacuum vessel is divided into two sub-tori with an electrical isolation material, G10, sandwiched between them. The electrical break is discussed in more detail in Section 2.3. The inner diameter (ID), outer diameter (OD) and wall thickness of the torus are 388 mm, 1212 mm, and 6 mm, respectively. The total interior volume (or, vacuum volume) of the vessel is 0.8 m^3 . A combination of circular, rectangular and trapezoidal ports, 22 in total, are present on the vacuum vessel. The description of various ports and their utility is presented in Section 2.2.1. The vacuum vessel is made of stainless steel 304L.

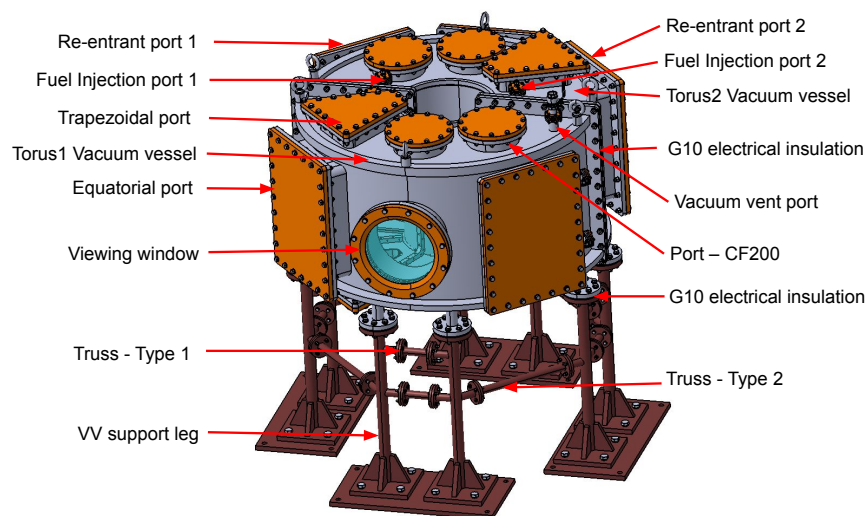


Figure 2: 3D CAD model of the PRAGYA vacuum vessel (VV) assembly.

Geometric feature	Value
Major radius, R_0	0.4 m
Minor radius, a	0.13 m – 0.18 m
Aspect ratio, A	2.22 – 3.15
Elongation, κ	1.55 – 2.20
Triangularity, δ	0.0 – 0.4

Table 1: Geometric features of the plasma in PRAGYA vacuum vessel

A	$\delta = 0$		$\delta = 0.4$	
	q_0	q_{95}	q_0	q_{95}
2.22	1.64	3.60	1.47	4.30
3.15	1.59	2.68	1.37	3.10

Table 2: The safety factor on the axis q_0 and at the edge q_{95} for the extreme values of the aspect ratio A and triangularity δ computed from the fixed-boundary Grad-Shafranov solver TokaMaker.

2.2. Design of the vacuum vessel

2.2.1. Ports

Each of the two sub-tori house multiple ports along the equatorial, top, and bottom sides. These ports will be used for diagnostics, connecting the pumping system, fuel inlet, and microwave heating source. The layout of the ports on the vacuum vessel is shown in Figure 2 and Figure 3 with a brief description of all the ports provided below.

Viewing port. A circular viewing port (diameter = 300 mm) is provided in the equatorial direction (shown in Figure 2, 3). The viewing port has a 20 mm thick toughened glass with O-ring sealing provided on the vacuum and atmosphere sides. This port provides visual access to high-speed cameras or for capturing plasma emissions using photomultiplier tubes (or photodiodes).

Trapezoidal-shaped port. A pair of trapezoidal ports are placed on the top and bottom sides of the vacuum vessel for diagnostics such as microwave interferometry. The trapezoidal shape allows a broader access in the radial direction and a closer reach on the inboard side of the vacuum vessel.

Diameter Nominal (DN) 200 ConFlat (CF) ports. Four DN 200 CF ports are provided on the top and one DN 200 CF port is provided bottom side of the vessel. The DN 200 ports placed on the top face of the vacuum vessel will be used for different diagnostics such as Langmuir probe. The bottom DN 200 port serves a dual purpose as a backup port for connecting the vacuum pump and as a port for diagnostics.

Gas injection port. Two DN 40 ports are placed on the top face of the vessel for gas injection (shown in Figure 2). A DN 3 SS304L ($OD = 10.3$ mm) pipe runs from each DN 40 CF port into the chamber while hugging along the wall (as shown in Figure 4a, 4c). These SS304L pipes run till the midplane and the gas is injected in the radial direction. To avoid vibrations of the inlet pipe during operations, they are held to the vacuum vessel using a clamp arrangement.

Equatorial rectangular port. A total of five identical rectangular ports are provided on the outboard side of the vessel along the toroidal direction. These ports are 340 mm in width and 500 mm in height. These ports have multiple utilities such as microwave injection, visualization and diagnostics. Figure 3 shows tangential entry port assembly in the PRAGYA vessel. The viewing port has toughened glass mounted on a DN 63 CF flange. The radial coverage of the tangential entry viewing port is 63 mm ranging from 384 mm till 447 mm.

Turbomolecular pump (TMP) port. A DN 160 CF port is placed on the bottom side of the vacuum vessel to connect a Pfeiffer HiPace 700 H turbomolecular pump (TMP) (as shown in Figure 3). The TMP is not directly mounted on the designated TMP port to avoid a large magnetic field protruding inside the TMP. The safe limit of external magnetic field for the TMP is 6 mT (provided in the operating instructions manual of Pfeiffer HiPace 700¹). Therefore, the TMP is placed 2 m away from the centerline of the vessel via an L-shaped bellow connected to the TMP port on the vessel. Based on the internal surface area (4.23 m²) and the total volume (0.8 m³) of the vacuum vessel along with the distance of the TMP from the vessel, reaching a vacuum of order 10^{-6} mbar will take approximately 20 hours. This can be reduced to 8 hours with the introduction of a booster pump.

Roughing pump port. Two DN 40 ports are placed on the bottom side of the vacuum vessel to connect Pfeiffer DuoVane 18 rotary vane pump (as shown in Figure

¹Pfeiffer HiPace 700 operating instructions manual

3). The details of the vacuum pumping are provided in Section 2.7.

Vacuum vent port. A DN 40 port is placed on the top side of the vacuum vessel for venting out the vacuum inside the vessel (as shown in Figure 2). For activities such as periodic maintenance and setting-up new diagnostics, the vessel needs to be purged and brought to atmospheric condition. Purging will be done by first ensuring all the pumps and gate valves are closed, and later injecting dry N_2 gas into the vessel.

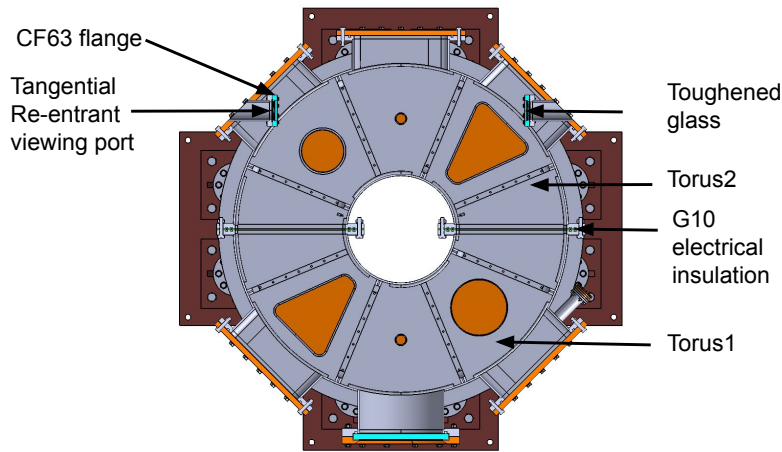


Figure 3: A cut-section view of the 3D CAD model of tangential viewing port in the PRAGYA vacuum vessel assembly.

2.3. Electrical break

The characteristic input current to the electrical coils responsible for magnetic field and plasma current involves current ramp-up and ramp-down stages. During the ramp-up or ramp-down stage, the change in magnetic flux leads to induced eddy current in the vacuum vessel walls. The induced eddy currents generate magnetic fields that interact with the plasma and affects its stability. In elongated tokamak plasmas, vertical stability is inherently unstable as any small vertical displacements grow exponentially without control (Fukuyama et al., 1975). Eddy currents in the vacuum vessel create up-down asymmetric radial fields that can either passively stabilize (reduce growth rate) or destabilize the plasma (worsen vertical instability and accelerate VDEs), depending on vessel geometry, time scale, and current mode. Furthermore in a toroidally continuous vacuum vessel, a major part of the Ohmic flux swing is lost in driving the current through the walls.

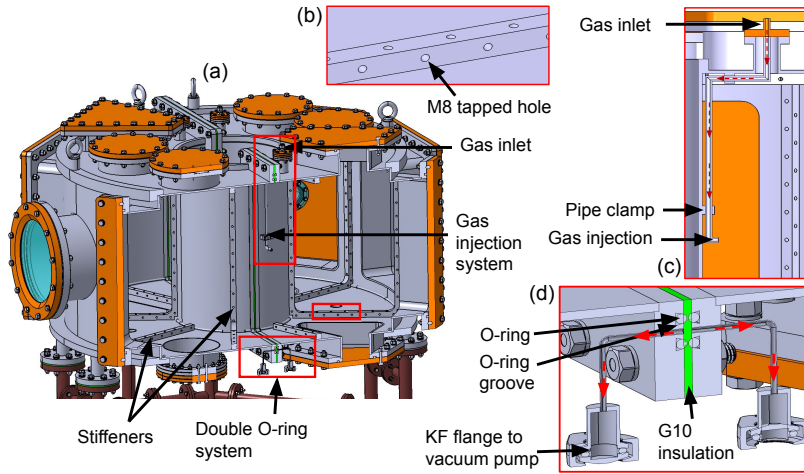


Figure 4: (a) A cut-section view of the 3D CAD model of the vacuum vessel assembly; zoomed-in descriptive view of (b) stiffener, (c) gas inlet system (dotted red arrows represent the direction of incoming gas flow), (d) double O-ring vacuum sealant assembly (dotted magenta arrows represent the direction of flow due to vacuum produced between the two O-ring arrangement).

This could be problematic in small machines where the available volt-seconds are minimal to start with. To minimize these effects, the vessel is divided into two sub-tori along the toroidal direction. A similar approach has been followed in existing tokamaks such as ADITYA-U (Jadeja et al., 2017), SUNIST (Li et al., 2015) and ASDEX (Finkelmeyer et al., 1979). An electrical insulation material G10, is sandwiched between the two sub-tori to provide electrical insulation in the toroidal direction. Figures 2 and 4d show the placement of G10 material in between the two torus. Additional G10 insulation is provided between the vessel and the support structure, as shown in Figure 2, to further minimize eddy currents.

To ensure a good vacuum sealing at the junction where the two sub-tori are placed together (with G10 in between them), the flanges of the two sub-tori are provided with a double O-ring arrangement as shown in Figures 4a and 4d. A series of two additional O-rings are placed along the poloidal direction and the space between them is evacuated using a roughing pump. The vacuum in this space will be maintained between 10^{-2} and 10^{-3} mbar. This will ensure that any atmospheric gas passing through the outer O-ring will be evacuated in the space between the two O-rings.

2.4. Stiffeners

The vacuum facing side of each tori houses ribs running along the poloidal direction. Figures 4a, 4b show the stiffeners in the vacuum vessel assembly. Although the addition of these ribs reduces the available volume for plasma, these ribs act as stiffeners providing structural rigidity to the vessel. These ribs have a cross-section $20 \times 20 \text{ mm}^2$. A total of eight ribs are present in the toroidal direction. Eight stiffeners are added on the top plate, bottom plate and outer cylinder. All these stiffeners are present on the inner faces. Four stiffeners are present on the inner face of inner cylinder. Furthermore, these ribs are lined with standard M8 tapped holes on three sides which will be used to mount limiter or diagnostic equipment inside the vacuum vessel. These tappings are 50 mm apart and are staggered on the adjacent faces. Figure B.1 in Appendix B shows a comparison of stress induced on a vacuum vessel with and without stiffeners. With the addition of stiffeners, a 6 to 7 times reduction in the maximum stress is observed.

2.5. Vacuum vessel support structure

The vacuum vessel rests on a support structure that consists of 8 legs (4 on each sub-torus). The legs are 0.75 m tall which puts the center of the circular viewing port 1.2 m above the ground. These legs are connected to the vessel at 620 mm away from the central axis to provide sufficient space at the bottom side of the vessel connecting vacuum pumps and diagnostics. These legs rest on base plate which will be grouted to the floor of the facility. The support legs are designed to hold the weight of the vessel without undergoing buckling. The details of linear buckling analysis performed on the support legs are provided in the Section 3.5.1. The legs are connected through trusses in the toroidal direction to give stability to the vessel against the lateral forces or moments acting onto it.

2.6. Material for construction

A common choice for the tokamak vacuum vessels is stainless steel due to its non-magnetic nature, good machinability characteristics, lower cost and corrosion resistance. The two widely used grades of stainless steel in the construction of tokamak vacuum vessels are 304 (L) (Ying et al., 2003; Song et al., 2006; Jadeja et al., 2017; Sontag et al., 2022) and 316 (L) (Sakurai et al., 2009; Mardani et al., 2012; Chung et al., 2013; Mancini et al., 2021; Huang et al., 2024) which differ by their corrosion resistance properties and the amount of carbon present in them. The vacuum vessel, ports, blanks of the ports, support structures are all made of SS304L. SS304L is chosen due to its lower magnetic permeability, high mechanical strength, corrosion resistance, low electrical conductivity, ease

of availability, established fabrication/machining processes and also the relatively low cost compared to SS316.

In summary, the key characteristics of the PRAGYA vacuum vessel assembly are listed below.

- i. The vacuum vessel is electrically isolated from the induced eddy current in the toroidal direction by dividing it into two sections.
- ii. To reduce leaks, a double O-ring arrangement is designed on the flanges and the space between the two sets of O-rings is evacuated using a vacuum pump.
- iii. Multiple ports are present on the equatorial, top and bottom sides of the vacuum vessel.
- iv. Use of ribs (or, stiffeners) to provide additional structural strength to the vacuum vessel which allows for mounting limiter or diagnostics inside the vacuum vessel.

2.7. *Vacuum pumping system*

The PRAGYA vacuum vessel is designed for a maximum vacuum of 10^{-6} mbar. To generate a vacuum of this order, a series of two pumps, a roughing pump (Pfeiffer Duovane 18 rotary vane pump²) of capacity 3.9 l/s and a turbomolecular pump (TMP) (Pfeiffer HiPace 700 H³) of capacity 665 l/s, are used. The TMP is connected to the bottom face of the vessel in the designated DN 160 CF port. The CF has a knife edge and an OFHC copper gasket to provide a vacuum seal. A splinter plate and a manual/electropneumatic gate valve is provided in between the DN 160 port and the TMP. The splinter plate prevents any unwanted material dropping into the TMP. The gate valve provides control to connect/disconnect the TMP from the vessel. The RVP is connected to the DN 40 CF port at the bottom face of the vacuum vessel.

3. **Thermo-mechanical stress analysis**

During operation, the vacuum vessel will be subjected to different loads,

- i. pressure differential due to vacuum inside the vacuum vessel and atmospheric pressure outside the vacuum vessel,
- ii. weight of the vessel,

²Pfeiffer Duovane 18 rotary vane pump data sheet

³Pfeiffer HiPace 700 H data sheet

- iii. thermal load during baking and
- iv. electromagnetic load.

Different features of the vacuum vessel such as the wall thickness, stiffener locations and dimensions, radius of curvature of the edges of the ports, are designed such that the stress induced in the vacuum vessel due to all these loads combined is within the material’s yield strength (170 MPa for SS304L).

Finite element analysis (FEA) is performed on the entire vacuum vessel assembly (including ports and support structure) to compute the stresses induced due to the vacuum, self-weight and thermal loads using COMSOL Multiphysics 6.3. The governing equations pertinent to the results in this paper are presented in Appendix C. Table 3 shows the mechanical and thermal and properties of stainless steel SS304L used during the simulations (American Society of Mechanical Engineers, 2019). The values at 20 °C are used during simulations at room temperature conditions, while the values at 150 °C are used for simulations at baking conditions.

Property	Value at	
	20 °C	150 °C
Density, ρ (kg/m ³)	8030	8030
Young’s modulus (GPa)	195	186
Poisson’s ratio	0.31	0.31
Heat capacity at constant pressure, C_p (J/(kg · K))	472	510
Thermal conductivity, k (W/(m · K))	14.8	17.0
Coefficient of thermal expansion, α ($\times 10^{-6}$ 1/K)	15.3	16.6

Table 3: Mechanical, thermal and electrical properties of stainless steel SS304L used in the COMSOL simulations. The heat capacity at constant pressure, $C_p = k/(\rho\alpha)$.

3.1. Grid Refinement Study

A grid refinement study is performed to optimize the number of mesh elements used for the simulations. Figure 5 shows the 3D CAD model and the mesh used for the simulation. At multiple places in the geometry, quadrilateral mesh elements are used as they provide uniform and better control of spatial distribution of mesh elements. The small features of the vacuum vessel assembly such as radius of curvature of the ports, stiffeners, port thickness, blank thickness, are

locally resolved as shown in Figure 5c to accurately represent the stress and deformation. To perform the grid convergence study, global and local mesh element size were changed. For the tetrahedral elements, the global mesh elements size was modified while for the quadrilateral elements, the local mesh element size was modified. Two parameters, surface-averaged von Mises stress and line-averaged von Mises stress are the quantities of interest in this study. The surface averaged von Mises stress is monitored at three locations - top plate, bottom plate and out-board cylinder. At certain locations where the changes in geometry are not smooth enough, a localization (in one or two mesh elements) of stress is observed. In this work, the locations where the ports meet the vessel especially on the inboard side of the trapezoidal ports were observed to be the regions of high stress localization. This is a well-known numerical artefact which can be resolved with a finer mesh around the problem zone or by analyzing the data a few mesh elements away from the problem zone. In this work, this issue is remedied by computing the line-averaged von Mises stress at the inboard side of the trapezoidal port. In all the simulations, the quantities of interest converge to a residual error of the order of 10^{-9} . The effect of mesh resolution on these quantities is shown in Figure 6a and Figure 6b. In the absence of a known solution, the error is measured relative to the solution on the finest grid. These figures are semilog plots with the abscissa (or number of mesh elements) in the log scale. As expected, the relative error reduces with an increase in number of mesh elements or a reduction in the mesh volume. The reduction is quite steep up to about 700k elements after which the error plateaus. Therefore, the simulations discussed in subsequent sections is performed on the mesh with 1012k number of mesh elements. This mesh is shown in the Figure 5(b-c).

3.2. *Vacuum vessel wall thickness*

The effect of wall thickness over the maximum stress induced in the vacuum vessel is evaluated first to narrow down the wall thickness. A convergence study is performed to evaluate the optimum wall thickness for the vessel. The study is performed considering the pressure difference due to vacuum and atmosphere, and self weight of the vessel. Maximum von Mises stress induced on different faces (top plate, bottom plate, inner cylinder and outer cylinder) of the vessel is monitored. The geometry and the corresponding mesh for this study is shown in Appendix A. Figure 7 shows the variation of maximum von Mises stress induced at these surfaces with respect to different wall thickness. Two observations are made: first, the maximum von Mises stress induced on the different faces of the vessel increases with a decrease in wall thickness; and second, for a given wall

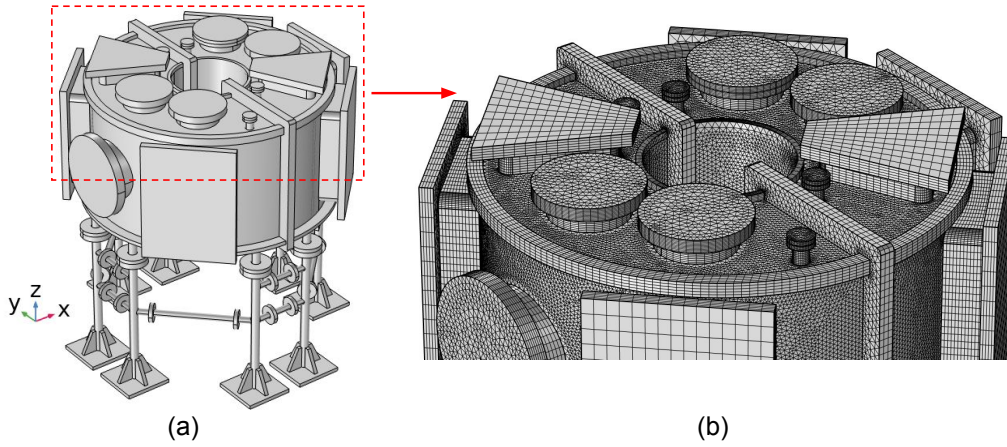


Figure 5: (a) 3D CAD model and (b) mesh used for the simulations.

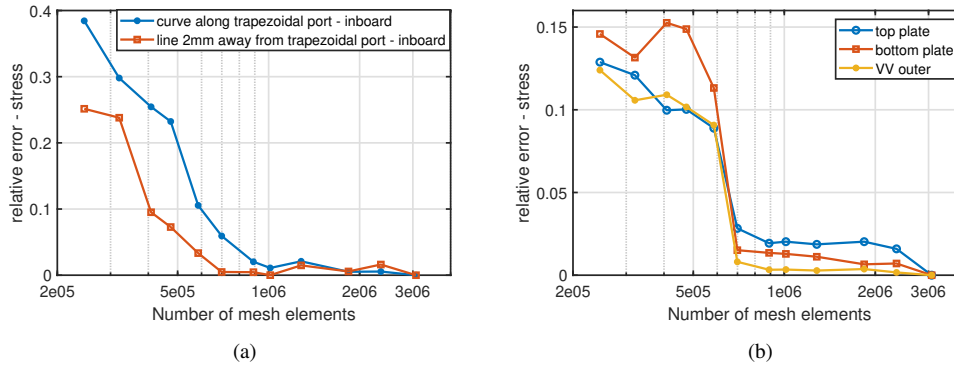


Figure 6: Semilogx plots of relative error in (a) von Mises stress averaged along a curve near the top trapezoidal port on the inboard side and (b) surface averaged von Mises stress averaged along top plate, bottom plate and vacuum vessel outer cylindrical surface.

thickness, the maximum von Mises stress is observed on the top plate except at higher wall thickness of 8 and 10 mm. Therefore, we consider the maximum stress induced on the top/bottom plate for the optimum wall thickness evaluation. It is observed that the maximum stress induced on a 4 mm thick vacuum vessel is approximately 200 MPa which is already quite close to the yield limit of SS304L. Increasing the wall thickness to 5 mm, 6 mm and 8 mm, induces a maximum stress of 123 MPa, 79 MPa and 51 MPa respectively. While the stress is considerably lower for both the 6 mm and the 8 mm thick wall, a 6 mm thick wall is chosen from a material volume and cost point of view.

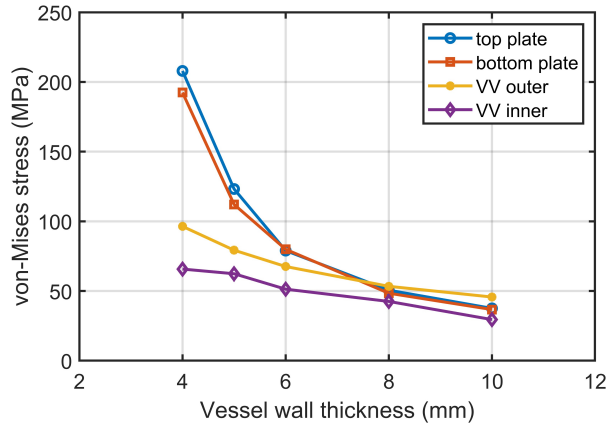


Figure 7: Wall thickness convergence study: Variation of peak von Mises stress at different surfaces of vacuum vessel vs vessel wall thickness.

3.3. Stress due to vacuum and self-weight of the vacuum vessel

To ascertain the structural integrity of the vacuum vessel against a differential pressure load due to vacuum, all the vacuum facing surfaces are set to a pressure of 10^{-5} Pa, while the atmosphere facing surfaces are set to a pressure of 101325 Pa. The base of the support legs are set to a fixed boundary condition with gravity acting along the negative z direction.

The resulting von Mises stress on the vessel due to the imposed pressure difference and self-weight of the vessel is shown in Figure 8. It is observed that the maximum stress induced on the vessel is around 110 MPa observed at two locations - one where the top trapezoidal port meets the vacuum vessel, and second on the inner faces where the stiffeners meet. The maximum deformation is observed to be around 0.5 mm at the bottom plate of the vessel where there are DN 40 ports. At all other surfaces, the stress is less than 40 MPa. The locations of maximum stress is observed to be mostly at places where the ports (trapezoidal or equatorial) meet the vessel. At these locations, a radius of curvature of 30 mm is added to relax the local stress concentration.

3.4. Stress due to baking at 150 °C

Upon exposure to the ambient environment, H_2O and H_2 molecules from the atmosphere get adsorbed in to the steel. During operations these gases release and contaminate the plasma generated from the fuel. To minimise the contamination, the vessel is baked at 150 °C for a duration of 48 hours before operations. This

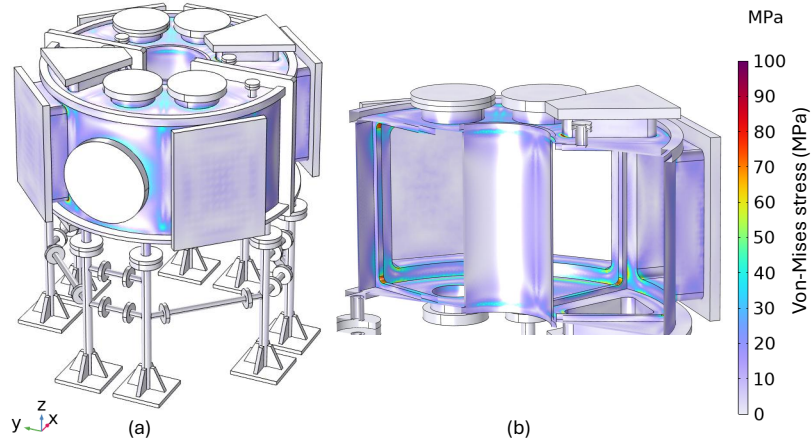


Figure 8: Spatial distribution of stress (von Mises) on the vacuum vessel due to vacuum and self-weight.

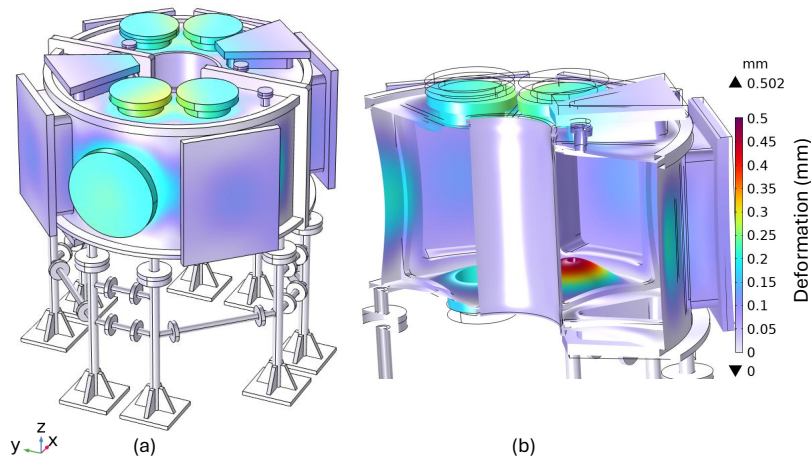


Figure 9: Spatial distribution of deformation (total) on the vacuum vessel due to vacuum and self-weight. In (b), the deformation is scaled 200 times for the ease of visualization.

removes most of the absorbed H_2O gas from the steel. However, heating the vessel to $150\text{ }^\circ\text{C}$ induces thermal stress which leads to the deformation of the vessel.

To assess the effect of baking on the structural integrity of the vacuum vessel, steady-state and transient thermoelastic (coupled heat transfer and structural deformation) simulations are performed to identify the regions of high stress and deformation. Upon fabrication, the PRAGYA vacuum vessel will be heated us-

ing infrared lamps (IR) on the vacuum facing surfaces. Therefore, in the current simulations, the vacuum facing surfaces are set to a heat flux boundary condition such that these surfaces reach a temperature of 150 °C. The heat flux is linearly varied with time such that the rate of temperature increase is limited to 5 °C per hour. After reaching 150 °C, the input heat flux is kept constant. The surfaces which are exposed to the atmosphere are set to a convective heat transfer boundary condition (with heat transfer coefficient, $h = 5 \text{ W}/(\text{m}^2 \cdot \text{K})$) to mimic natural convection. The base of the support legs are set to a fixed boundary condition. The temporal evolution of the surface-averaged temperature on the inner face of inner cylinder and inner face of outer cylinder is shown in Figure 10. It is observed that the temperature of these two surfaces increases steadily for 26 hours after which it becomes steady.

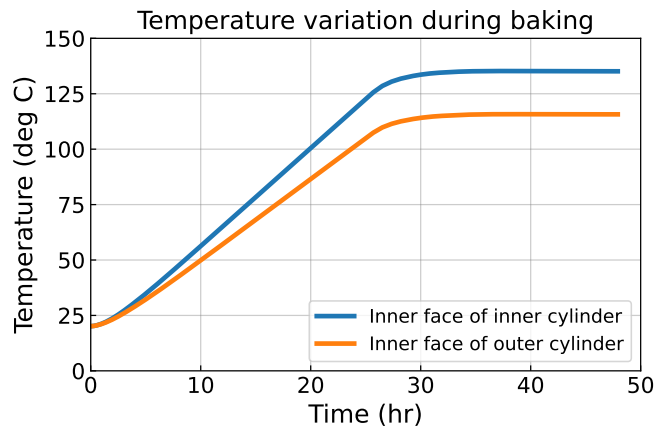


Figure 10: Temporal variation of surface-averaged temperature on the inner face of outer cylinder vacuum vessel due to vacuum, self-weight and baking at 150 °C.

The spatial distribution of temperature inside and outside the vacuum vessel is shown in Figure 11. Although all the vacuum-facing-surfaces are set to an uniform heat flux boundary condition, the temperature distribution is not uniform inside (or outside) the vacuum vessel. While at some spatial location, the temperature does reach (or exceeds) the desired baking temperature i.e. 150 °C, at other spatial location, the temperature lies between 100 and 140 °C. Figure 12 shows the variation of temperature in the radial direction along the top plate of the vacuum vessel from the inboard side to the outboard side. Since the vacuum vessel is baked at the inner vacuum-facing-surfaces and there is a convective heat transfer boundary condition applied on the outer faces of inboard and outboard

sides of the vacuum vessel, a slight drop in temperature is observed as we move away from plasma center to either side (inboard/outboard) of the vacuum vessel.

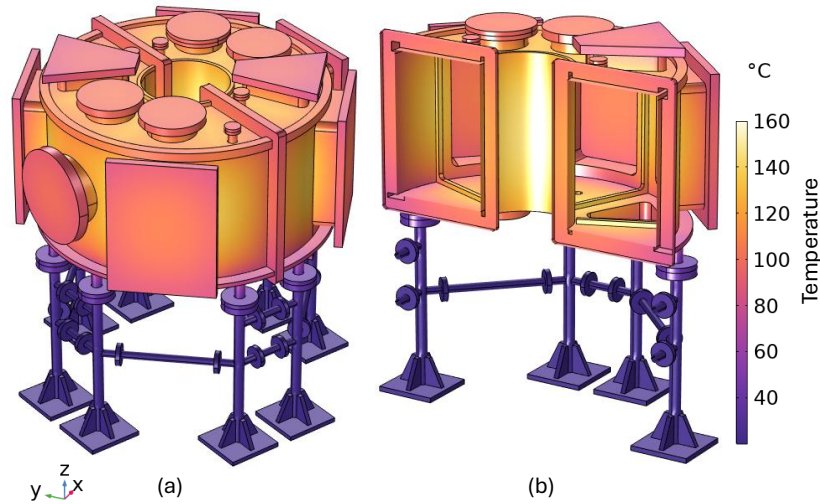


Figure 11: Spatial distribution of temperature on the vacuum vessel due to vacuum, self-weight and baking at 150 °C.

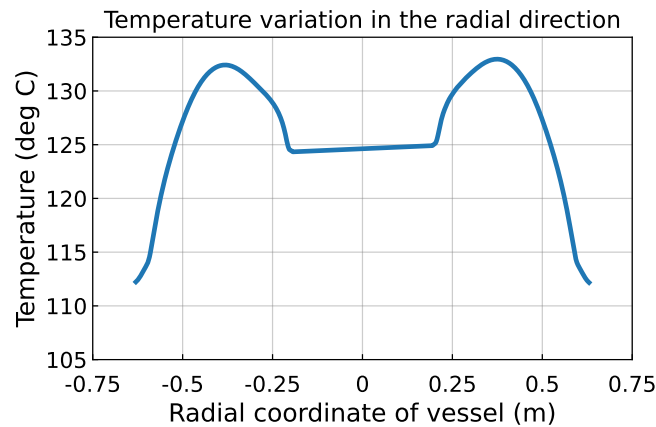


Figure 12: Variation of temperature in the radial direction at the top plate of the vacuum vessel during baking. Coordinate '0' corresponds to the center of the vacuum vessel.

The stress induced on the vacuum vessel due to simultaneous vacuum and thermal load is shown in Figure 13. The maximum stress induced is approximately

280 MPa at two locations - one, on the inboard side of the torus; and second, where the stiffener merges with the inner face of the vacuum vessel as shown in Figure 13b. However, since the thermal stress is considered as a secondary stress and not a primary stress, the acceptable stress values for the combined primary and secondary stress is twice the yield strength Santra et al. (2009); tao Song et al. (2006). Thus, according to ASME criteria, the maximum stress values are within the acceptable limits. On the rest of the vacuum vessel, the thermal stress is less than 80 MPa.

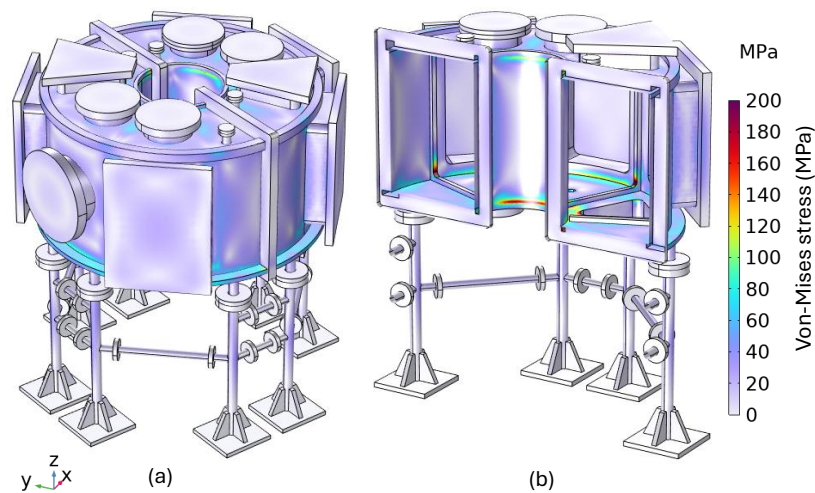


Figure 13: Spatial distribution of stress (Von Mises) on the vacuum vessel due to vacuum, self-weight and baking at 150 °C.

Figure 14 shows the spatial variation of deformation of the vacuum vessel assembly. Since, the base of the support leg is set to a fixed boundary condition, minimal thermal deformation is observed on the parts of the vacuum vessel close to the support leg, while maximum thermal deformation is observed at locations farthest from the support leg. The maximum deformation is observed to be around 2.1 mm at the top of the vacuum vessel.

Although, in the simulations the base of support leg is set to a fixed boundary condition, practically the vessel is not fixed to the base of the floor and has provision for slight movement and expansion. The support legs of the vacuum vessel will rest on larger flat base plates (to distribute the load on to larger surface area) which will be grouted to the floor of the laboratory. The support leg will be held onto the flat base plates using bolt arrangement using expandable washers, and

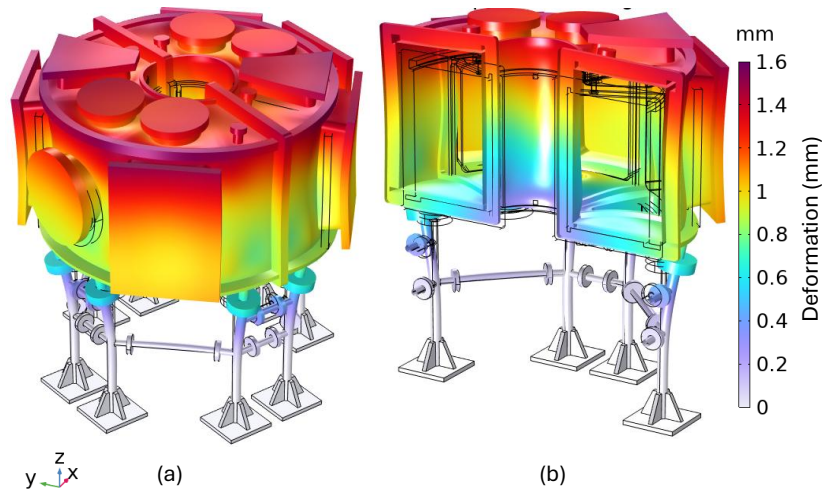


Figure 14: Spatial distribution of deformation (total) on the vacuum vessel due to vacuum, self-weight and baking at 150 °C. In (b), the deformation is scaled 100 times for the ease of visualization.

larger bolt hole size (1 mm larger) than the bolt nominal diameter. These characteristics will provide a flexibility to the support legs for slight movement, which will further reduce the induced thermal stress. The central flange that holds the two sub-tori will also have expandable washers and a larger bolt hole size (1 mm larger) to allow for thermal expansion.

3.5. Linear buckling analysis of the vessel and support legs

The vessel and the support legs are analysed for buckling due to different loads (weight and pressure difference). This is done to ensure that the structure does not undergo sudden collapse under varying loads acting on it. A linear buckling analysis is performed in two stages: first, one support leg is checked for buckling due to weight of the vessel acting on it; second, the entire vessel is checked for buckling both due to weight and pressure difference.

3.5.1. Linear buckling analysis of the support legs

A single support leg is checked for buckling due to the weight of the vessel acting on it. The support leg has an annular cross-section with an ID = 28 mm, OD = 48.30 mm and length = 700 mm. Equation 1 gives the critical load on a column that can lead to buckling,

$$P_{Cr} = \frac{\pi^2 EI}{(KL)^2} \quad (1)$$

where E , I , K and L are Young's modulus (200 GPa), minimum second area moment of inertia of the cross-section of the column, column effective length factor, and length of the column, respectively. Here, $K = 2$ considering the support leg is fixed at one end and free at the other end. Following Equation 1, the critical load on the support leg comes out to 23,866 kg. This provides a factor of safety of 120. Such a high factor of safety is considered here to allow the vessel withstand other loads acting on it during operations which are not considered here such as the non-uniformity in the placement and load distribution on each support leg, moment acting due to induced Lorentz forces, or a sudden collapse of any one support leg.

Figure 15 shows the 3D CAD, mesh and boundary conditions acting on the support leg during linear buckling analysis. The base of the support leg is set to a fixed constraint boundary condition, and a vertical load of 2 kN is applied on the top face of the support leg.

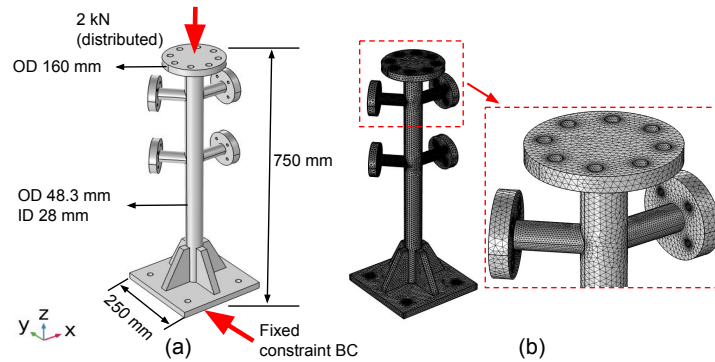


Figure 15: (a) 3D CAD model of the support leg and (b) mesh, during linear buckling analysis.

Figure 16 shows the different modes of deformation (or failure) and their corresponding critical load factor (CLF) during vertical load (weight of the vessel) on the support leg. It is observed that the CLF for all modes is greater than 100. This implies that the required load for the support leg to buckle is at least two orders of magnitude larger than the applied load of 2 kN, ensuring the support leg is stable during operations.

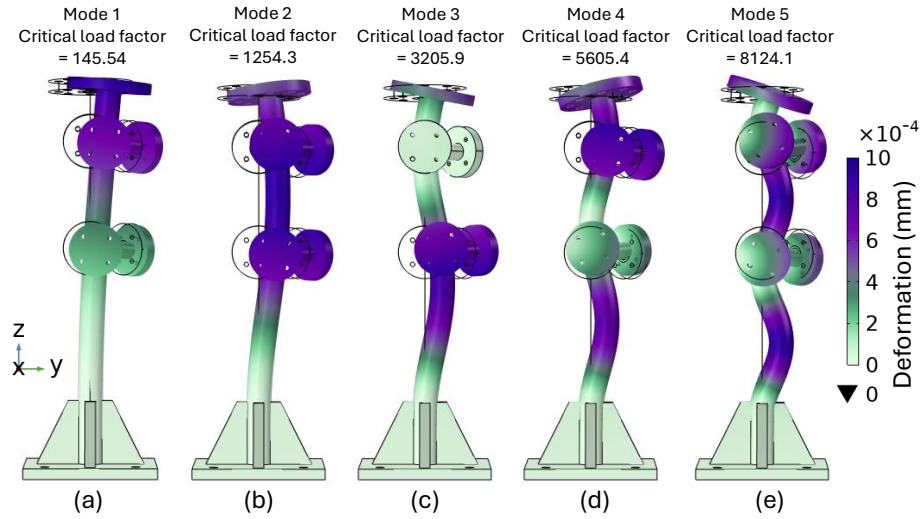


Figure 16: Different modes of deformation and their corresponding critical load factor during vertical load on the support leg (a) Mode 1, (b) Mode 2, (c) Mode 3, (d) Mode 4, and (e) Mode 5.

3.5.2. Linear buckling analysis of the vacuum vessel assembly

In this section, we discuss different modes of failure and their corresponding critical load factors of the entire vacuum vessel assembly due to self-weight and pressure difference. A pressure boundary condition ($P = 10^{-5}$ Pa) is applied to all the vacuum-facing-surfaces and atmospheric pressure ($P = 101325$ Pa) is applied to all the surfaces exposed to atmosphere. The base of the support leg is set to a fixed boundary condition and the gravity acts along the negative z direction. Figure 17 shows the different modes of failure and their corresponding CLF. It is observed that there are different modes through which the vacuum vessel can fail such as twisting of the vacuum vessel (mode 1, figure 17a), collapse (or large deformation) around the circular viewing port (mode 2, Figure 17b), large deformation at the bottom face of the vacuum vessel where there are two small DN 40 ports (mode 3, Figure 17c), or collapse across the central flange connecting the two torus (mode 4 and 8, Figure 17d, 17e). However, the CLF for all these modes is $\gg 1$ which ensures the stability of the vacuum vessel against the applied load.

The linear buckling analysis of the individual support leg and the vacuum vessel assembly shows that they are stable to buckling during self-weight and pressure difference load.

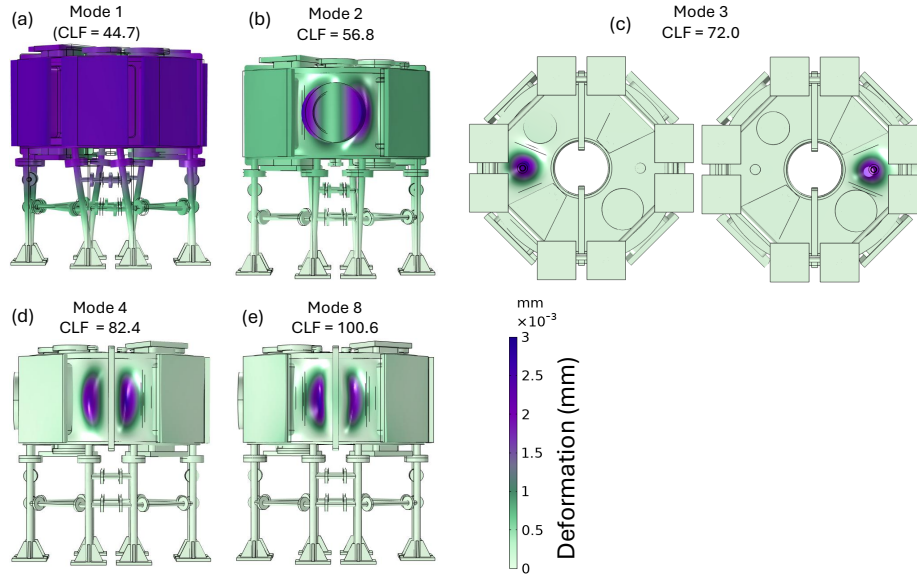


Figure 17: Different modes of deformation and their corresponding critical load factor (CLF) during vertical load on the support leg (a) Mode 1, (b) Mode 2, (c) Mode 3, (d) Mode 4, and (e) Mode 8.

4. Conclusions

The paper presents the design of the vacuum vessel assembly of the low aspect ratio tokamak- PRAGYA designed by Pranos Fusion Energy, based in Bangalore, India. The design primarily focuses on the structural and thermal loads acting on the vacuum vessel. PRAGYA tokamak is designed for a plasma major radius of 0.4 m, a plasma minor radius > 0.18 m and a plasma current of up to 25 kA. The PRAGYA vacuum vessel has a few distinctive features such as - presence of multiple ports, presence of a toroidal electric break to minimize the induced eddy current on the vacuum vessel, a double O-ring arrangement to minimize the vacuum leak, and stiffeners on the inner face of the vacuum vessel which provide strength to the vessel and have facility to house limiters. Structural, thermal, and linear buckling analysis of the vacuum vessel assembly is performed to identify the load bearing capacity of the vacuum vessel against pressure differential, self-weight and thermal load (due to baking at 150 °C). It is observed that the stress induced on the vacuum vessel due to pressure and thermal load are within the acceptable limit (less than the yield strength of SS304 L). The maximum stress developed on the vessel is around 110 MPa due to vacuum and self-weight load;

with the maximum deformation of 0.5 mm observed on the bottom side of the vacuum vessel. During baking, a maximum stress of 280 MPa is observed on the inboard side of the vacuum vessel. Considering thermal stress as secondary stress, the maximum stress is within the acceptable limit. The linear buckling analysis of the individual support leg and the vacuum vessel assembly shows that they are stable to buckling during self-weight and pressure difference load. Future work will consider the effects of electromagnetic load during normal and disruptive events on the vacuum vessel.

Appendix A. Vacuum vessel wall thickness optimization - Geometry and Mesh

This section shows the geometry and the corresponding mesh used during the wall thickness optimization study discussed in Section 3. In the geometry used for optimization study, in addition to the toroidal vacuum vessel, the slots for the ports are provided on different faces of the vacuum vessel. In addition, stiffeners were added on the inside of the vessel. Eight stiffeners are added on each of the following surfaces - top plate, bottom plate and outer cylinder. These stiffeners are present on the inner faces. Four stiffeners are present on the inner face of the inner cylinder. More details on the stiffener can be found in the Section 2.4. During the wall thickness optimization, the geometry is kept same, only the wall thickness is varied. Figure A.1 shows the geometry and corresponding mesh for case: 6 mm wall thickness.

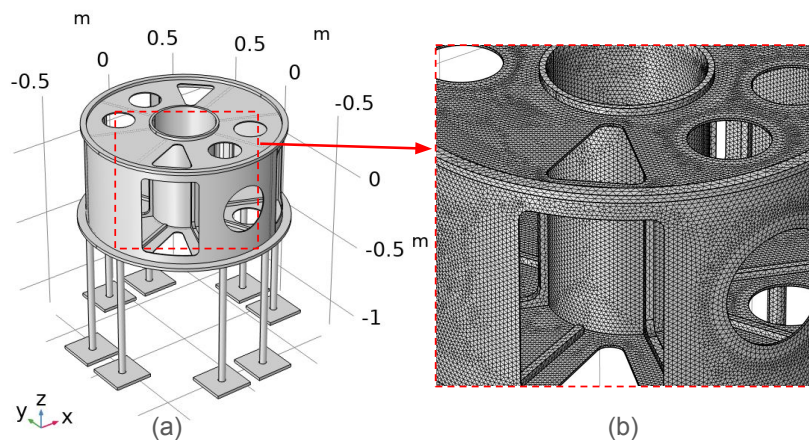


Figure A.1: Geometry and mesh used for the wall thickness optimization study.

Appendix B. Mechanical analysis with and without stiffeners

This section shows a comparison between the mechanical response of the vacuum vessel with and without the stiffeners. The comparison is made for the vessel wall thickness of 6 mm. It is observed that adding stiffeners to different faces of vessel results in significant reduction in the observed values of maximum stress. The maximum stress on the cylindrical face of the vacuum vessel reduces from approximately 400 MPa to 60 MPa. This is shown in Figure B.1. Thus, it is observed that stiffeners are useful in reducing stress levels in the vacuum vessel. Without stiffeners, a thicker vessel will be required to handle such large stress values on the vacuum vessel

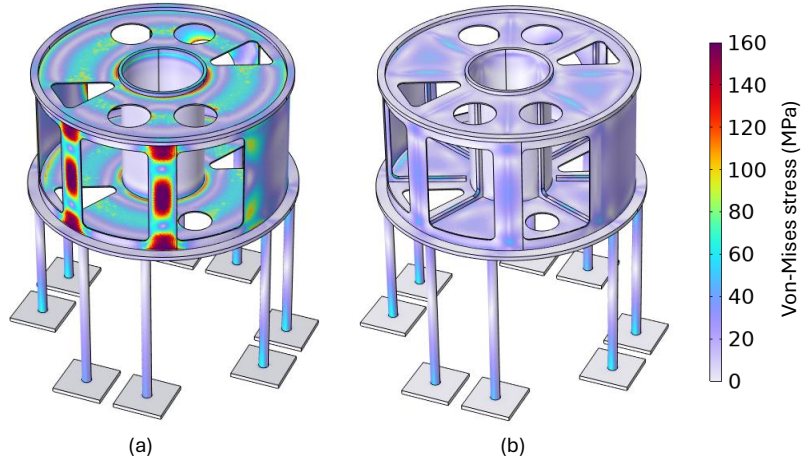


Figure B.1: Comparison of von-Mises stress induced on the vacuum vessel (a) without stiffeners, and (b) with stiffeners; Case = 6 mm wall thickness.

Appendix C. Governing Equations

The governing equations corresponding to the structural⁴ and themomechanical⁵ analysis of the vacuum vessel in COMSOL Multiphysics 6.3 and the fixed-boundary equilibrium in TokaMaker (Hansen et al., 2024) are described in this appendix.

⁴COMSOL 6.3 Structural Mechanics Module User's Guide

⁵COMSOL 6.3 Heat Transfer Module User's Guide

Solid deformation. The equation of motion of the solid body displacement \mathbf{u} in terms of the Cauchy stress tensor $\boldsymbol{\sigma}$ is given by

$$\rho \frac{\partial^2 \mathbf{u}}{\partial t^2} = \nabla \cdot \boldsymbol{\sigma} + \mathbf{f}_V \quad (\text{C.1})$$

where ρ is the density and \mathbf{f}_V is the external volume force vector of the deformed solid body. For a linear elastic material, the stress tensor is given by

$$\boldsymbol{\sigma} = \mathbf{C} : \boldsymbol{\varepsilon} \quad (\text{C.2})$$

where $\boldsymbol{\varepsilon}$ is the strain tensor, \mathbf{C} is the fourth-order elasticity tensor and ":" indicates a contraction operation over two indices. For an isotropic material, \mathbf{C} reduces to a 6×6 matrix known as an elasticity matrix \mathbf{D} which is given by

$$\mathbf{D} = \frac{E}{(1+\nu)(1-2\nu)} \begin{bmatrix} 1-\nu & \nu & \nu & 0 & 0 & 0 \\ \nu & 1-\nu & \nu & 0 & 0 & 0 \\ \nu & \nu & 1-\nu & 0 & 0 & 0 \\ 0 & 0 & 0 & \frac{1-2\nu}{2} & 0 & 0 \\ 0 & 0 & 0 & 0 & \frac{1-2\nu}{2} & 0 \\ 0 & 0 & 0 & 0 & 0 & \frac{1-2\nu}{2} \end{bmatrix} \quad (\text{C.3})$$

where E is the Young's modulus and ν is the Poisson's ratio.

The Cauchy stress can be decomposed into isotropic and deviatoric stresses where pressure forms the volumetric isotropic part such that

$$p = -\frac{1}{2} \text{trace}(\boldsymbol{\sigma}) \quad (\text{C.4})$$

and the deviatoric part is defined as

$$\boldsymbol{\sigma}_d = \boldsymbol{\sigma} + p\mathbf{I}. \quad (\text{C.5})$$

The von Mises stress is computed from the second invariant of $\boldsymbol{\sigma}_d$ such that

$$\sigma_{\text{mises}} = \sqrt{\frac{3}{2} \boldsymbol{\sigma}_d : \boldsymbol{\sigma}_d} \quad (\text{C.6})$$

Heat transfer in solids. The heat transfer in solids is given by

$$\rho C_p \left(\frac{\partial T}{\partial t} + \mathbf{u} \cdot \nabla T \right) + \nabla \cdot \mathbf{q} = -\alpha T : \frac{dS}{dt} + Q \quad (\text{C.7})$$

where ρ is the solid density, C_p is the specific heat capacity at constant pressure, T is the temperature, \mathbf{u} is the translational velocity, \mathbf{q} is the conduction heat flux, α is the coefficient of thermal expansion, S is the second Piola-Kirchoff stress tensor and Q represents additional volumetric heat sources. Following the Fourier's law of heat conduction, $\mathbf{q} = -k\nabla T$ where k is the thermal conductivity of the solid. The first term on the right hand side of the equation is the thermoelastic damping. The Cauchy stress tensor σ and S are related by

$$\sigma = J^{-1}FSF^T \quad (\text{C.8})$$

where the deformation gradient tensor $F = \nabla\mathbf{u} + \mathbf{I}$ and the ratio between the current and initial mass density is given by $J = \det(F)$. In the coupled system, the solid body experiences additional thermal strain ε_{Th} which is given by

$$\varepsilon_{\text{Th}} = \alpha\Delta T \quad (\text{C.9})$$

where α is the coefficient of thermal expansion and ΔT is change in temperature of the solid body. The resulting constitutive relation is now given by

$$\sigma = \mathbf{C} : (\varepsilon - \varepsilon_{\text{Th}}). \quad (\text{C.10})$$

Grad-Shafranov equation. The Grad-Shafranov equation describes a plasma under static hydrodynamic equilibrium wherein the plasma pressure is balanced by external magnetic field. This is a non-linear elliptic partial differential equation derived in axisymmetric cylindrical coordinates and is given by

$$R \frac{\partial}{\partial R} \left(\frac{1}{R} \frac{\partial \psi}{\partial R} \right) + \frac{\partial^2 \psi}{\partial Z^2} = -\mu_0 R J_\phi(R, Z) \quad (\text{C.11})$$

where ψ is the poloidal flux function (V.s/rad), J_ϕ is the toroidal current density (A/m²), μ_0 is the permeability of free space. The toroidal current density J_ϕ is given by

$$J_\phi = R \frac{dp}{d\psi} + \frac{1}{\mu_0 R} F(\psi) \frac{dF}{d\psi} \quad (\text{C.12})$$

where p is the isotropic plasma pressure (Pa) and F is the toroidal field function defined as $F = RB_\phi$ (T.m) where B_ϕ is the toroidal magnetic field (T).

References

J. D. Lawson, Some criteria for a power producing thermonuclear reactor, Proceedings of the physical society. Section B 70 (1957) 6.

- ITER Physics Expert Group on Confinement and Transport and ITER Physics Expert Group on Confinement Modelling and Database and ITER Physics Basis Editors, Chapter 2: Plasma confinement and transport, *Nuclear Fusion* 39 (1999) 2175. URL: <https://doi.org/10.1088/0029-5515/39/12/302>. doi:10.1088/0029-5515/39/12/302.
- W. Horton, Drift waves and transport, *Rev. Mod. Phys.* 71 (1999) 735–778. URL: <https://link.aps.org/doi/10.1103/RevModPhys.71.735>. doi:10.1103/RevModPhys.71.735.
- T. Hender, J. Wesley, J. Bialek, A. Bondeson, A. Boozer, R. Buttery, A. Garofalo, T. Goodman, R. Granetz, Y. Gribov, et al., MHD stability, operational limits and disruptions, *Nuclear fusion* 47 (2007) S128.
- G. Federici, C. H. Skinner, J. N. Brooks, J. P. Coad, C. Grisolia, A. A. Haasz, A. Hassanein, V. Philipps, C. S. Pitcher, J. Roth, et al., Plasma-material interactions in current tokamaks and their implications for next step fusion reactors, *Nuclear Fusion* 41 (2001) 1967.
- A. Herrmann, Overview on stationary and transient divertor heat loads, *Plasma Physics and Controlled Fusion* 44 (2002) 883. URL: <https://doi.org/10.1088/0741-3335/44/6/318>. doi:10.1088/0741-3335/44/6/318.
- M. Keilhacker, JET deuterium: tritium results and their implications, *Philosophical Transactions of the Royal Society of London. Series A: Mathematical, Physical and Engineering Sciences* 357 (1999) 415–442.
- J. Strachan, S. Batha, M. Beer, M. Bell, R. Bell, A. Belov, H. Berk, S. Bernabei, M. Bitter, B. Breizman, et al., TFTR DT experiments, *Plasma Physics and Controlled Fusion* 39 (1997) B103.
- H. Kishimoto, S. Ishida, M. Kikuchi, H. Ninomiya, Advanced tokamak research on JT-60, *Nuclear fusion* 45 (2005) 986.
- F. Wagner, G. Becker, K. Behringer, D. Campbell, A. Eberhagen, W. Engelhardt, G. Fussmann, O. Gehre, J. Gernhardt, G. v. Gierke, et al., Regime of improved confinement and high beta in neutral-beam-heated divertor discharges of the asdex tokamak, *Physical Review Letters* 49 (1982) 1408.

- A. Darke, J. Harbar, J. Hay, J. Hicks, J. Hill, J. McKenzie, A. Morris, M. Nightingale, T. Todd, G. Voss, J. Watkins, MAST: A Mega Amp Spherical Tokamak, *Fusion Technology* 1994 (1995) 799–802. doi:10.1016/b978-0-444-82220-8.50167-9.
- M. Ono, M. Bell, R. Bell, T. Bigelow, M. Bitter, W. Blanchard, D. Darrow, E. Fredrickson, D. Gates, L. Grisham, et al., Overview of the initial NSTX experimental results, *Nuclear fusion* 41 (2001) 1435.
- Z. S. Hartwig, R. F. Vieira, D. Dunn, T. Golfinopoulos, B. LaBombard, C. J. Lammi, P. C. Michael, S. Agabian, D. Arsenault, R. Barnett, et al., The SPARC toroidal field model coil program, *IEEE Transactions on Applied Superconductivity* 34 (2023) 1–16.
- D. Whyte, B. LaBombard, J. Doody, T. Golfinopoulos, R. Granetz, C. Lammi, S. Lane-Walsh, P. Michael, T. Mouratidis, R. Mumgaard, et al., Experimental assessment and model validation of the SPARC toroidal field model coil, *IEEE Transactions on Applied Superconductivity* 34 (2023) 1–18.
- G. M. Staebler, M. Knolker, P. Snyder, C. Angioni, E. Fable, T. Luda, C. Bourdelle, J. Garcia, J. Citrin, M. Marin, et al., Advances in prediction of tokamak experiments with theory-based models, *Nuclear Fusion* 62 (2022) 042005.
- B. Lyons, J. McClenaghan, T. Slendebroek, O. Meneghini, T. Neiser, S. Smith, D. Weisberg, E. Belli, J. Candy, J. Hanson, et al., Flexible, integrated modeling of tokamak stability, transport, equilibrium, and pedestal physics, *Physics of Plasmas* 30 (2023).
- F. Jenko, Accelerating fusion research via supercomputing, *Nature Reviews Physics* 7 (2025) 365–377. URL: <https://doi.org/10.1038/s42254-025-00837-1>. doi:10.1038/s42254-025-00837-1.
- J. Degrave, F. Felici, J. Buchli, M. Neunert, B. Tracey, F. Carpanese, T. Ewalds, R. Hafner, A. Abdolmaleki, D. de las Casas, C. Donner, L. Fritz, C. Galperti, A. Huber, J. Keeling, M. Tsimpoukelli, J. Kay, A. Merle, J.-M. Moret, S. Noury, F. Pesamosca, D. Pfau, O. Sauter, C. Sommariva, S. Coda, B. Duval, A. Fasoli, P. Kohli, K. Kavukcuoglu, D. Hassabis, M. Riedmiller, Magnetic control of tokamak plasmas through deep reinforcement learning, *Nature* 602 (2022) 414–419. URL: <https://doi.org/10.1038/s41586-021-04301-9>. doi:10.1038/s41586-021-04301-9.

- S. Kerboua-Benlarbi, R. Nouailletas, B. Faugeras, E. Nardon, P. Moreau, Magnetic control of WEST plasmas through deep reinforcement learning, *IEEE Transactions on Plasma Science* 52 (2024) 3698–3703. doi:10.1109/TPS.2024.3377811.
- R. L. Miller, Y. R. Lin-Liu, A. D. Turnbull, V. S. Chan, L. D. Pearlstein, O. Sauter, L. Villard, Stable bootstrap-current driven equilibria for low aspect ratio tokamaks, General Atomics, San Diego, CA (United States); Lawrence Berkeley Lab., CA (United States), 1996. URL: <https://www.osti.gov/biblio/390606>.
- A. C. Sontag, M. W. Bongard, M. T. Borchardt, S. J. Diem, R. J. Fonck, A. K. Keyhani, B. A. Kujak-Ford, B. T. Lewicki, M. D. Nornberg, A. C. Palmer, et al., The new PEGASUS-III experiment, *IEEE Transactions on Plasma Science* 50 (2022) 4009–4014.
- W. Ying, Z. Li, H. Yexi, S. Team, et al., Initial plasma startup test on SUNIST spherical tokamak, *Plasma Science and Technology* 5 (2003) 2017.
- T. Maekawa, Y. Terumichi, H. Tanaka, M. Uchida, T. Yoshinaga, S. Yamaguchi, H. Igami, M. Konno, K. Katsuura, K. Hayashi, et al., Formation of spherical tokamak equilibria by ECH in the LATE device, *Nuclear fusion* 45 (2005) 1439.
- D. P. Boyle, J. Anderson, S. Banerjee, R. Bell, W. Capecchi, D. Elliott, C. Hansen, S. Kubota, B. LeBlanc, A. Maan, et al., Extending the low-recycling, flat temperature profile regime in the lithium tokamak experiment- β (LTX- β) with ohmic and neutral beam heating, *Nuclear Fusion* 63 (2023) 056020.
- S. Banerjee, D. Boyle, A. Maan, N. Ferraro, G. Wilkie, R. Majeski, M. Podesta, R. Bell, C. Hansen, W. Capecchi, et al., Investigating the role of edge neutrals in exciting tearing mode activity and achieving flat temperature profiles in LTX- β , *Nuclear Fusion* 64 (2024) 046026.
- Y.-K. Peng, The physics of spherical torus plasmas, *Physics of Plasmas* 7 (2000) 1681–1692.
- M. Ono, R. Kaita, Recent progress on spherical torus research, *Physics of Plasmas* 22 (2015).

- S. Wu, E. team, et al., An overview of the EAST project, *Fusion Engineering and Design* 82 (2007) 463–471.
- S. Deshpande, SST-1: an overview, in: 17th IEEE/NPSS Symposium Fusion Engineering (Cat. No. 97CH36131), volume 1, IEEE, 1997, pp. 227–232.
- J. Bucalossi, J. Achard, O. Agullo, T. Alarcon, L. Allegretti, H. Ancher, G. Antar, S. Antusch, V. Anzallo, C. Arnas, et al., Operating a full tungsten actively cooled tokamak: overview of west first phase of operation, *Nuclear Fusion* 62 (2022) 042007.
- J. L. Luxon, A design retrospective of the DIII-D tokamak, *Nuclear Fusion* 42 (2002) 614.
- V. Tomarchio, P. Barabaschi, E. Di Pietro, M. Hanada, Y. Kamada, A. Sakasai, H. Shirai, Status of the JT-60SA project: An overview on fabrication, assembly and future exploitation, *Fusion Engineering and Design* 123 (2017) 3–10. URL: <https://www.sciencedirect.com/science/article/pii/S0920379617305859>. doi:<https://doi.org/10.1016/j.fusengdes.2017.05.041>, proceedings of the 29th Symposium on Fusion Technology (SOFT-29) Prague, Czech Republic, September 5-9, 2016.
- S. Bhatt, D. Bora, B. Buch, , et al., Aditya : the first indian tokamak, *Indian Journal of Pure and Applied Physics* 27 (1989) 710–742.
- E. S. Marmor, A. C.-M. Group, The Alcator C-Mod program, *Fusion science and technology* 51 (2007) 261–265.
- A. Creely, M. J. Greenwald, S. B. Ballinger, D. Brunner, J. Canik, J. Doody, T. Fülöp, D. Garnier, R. Granetz, T. Gray, et al., Overview of the SPARC tokamak, *Journal of Plasma Physics* 86 (2020) 865860502.
- G. Lee, M. Kwon, C. Doh, B. Hong, K. Kim, M. Cho, W. Namkung, C.-S. Chang, Y. Kim, J. Kim, et al., Design and construction of the KSTAR tokamak, *Nuclear Fusion* 41 (2001) 1515.
- C. Wong, J. Wesley, R. Stambaugh, E. Cheng, Toroidal reactor designs as a function of aspect ratio and elongation, *Nuclear Fusion* 42 (2002) 547. URL: <https://doi.org/10.1088/0029-5515/42/5/307>. doi:10.1088/0029-5515/42/5/307.

- C. Hansen, I. Stewart, D. Burgess, M. Pharr, S. Guizzo, F. Logak, A. Nelson, C. Paz-Soldan, TokaMaker: An open-source time-dependent grad-shafranov tool for the design and modeling of axisymmetric fusion devices, *Computer Physics Communications* 298 (2024) 109111. URL: <https://www.sciencedirect.com/science/article/pii/S0010465524000341>. doi:<https://doi.org/10.1016/j.cpc.2024.109111>.
- A. Fukuyama, S. Seki, H. Momota, R. Itatani, Positional instabilities in a tokamak with a resistive shell, *Japanese Journal of Applied Physics* 14 (1975) 871.
- K. Jadeja, S. Bhatt, K. Rathod, K. Patel, V. Prajapati, K. Acharya, N. Patel, R. Tanna, M. Kalal, J. Ghosh, et al., ADITYA upgrade vacuum vessel: Design, construction, testing, installation and operation, *Fusion Engineering and Design* 124 (2017) 558–561.
- G. Li, Y. Tan, Y. Liu, Measurement of eddy-current distribution in the vacuum vessel of the Sino-UNited Spherical Tokamak, *Review of scientific instruments* 86 (2015).
- H. Finkelmeyer, J. Franzspeck, J. Gernhardt, F. Gresser, G. Haas, F. Hartz, G. Herppich, M. Keilhacker, G. Klement, M. Kornherr, Assembly and commissioning of the ASDEX tokamak, in: *8th Symposium on Engineering Problems of Fusion Research*, volume 3, 1979, pp. 1299–1302.
- Y. Song, D. Yao, Z. Liao, J. Yu, H. Xie, W. Wu, D. Gao, S. Wu, J. Li, P. Weng, et al., Design, fabrication and testing results of vacuum vessel, thermal shield and cryostat of EAST, in: *21th International Atomic Energy Agency Fusion Energy Conference in Cheng Du, China 16-21 Oct, 2006*.
- S. Sakurai, K. Masaki, Y. K. Shibama, A. Sakasai, Design and manufacturing of vacuum vessel for JT-60SA, *Fusion engineering and design* 84 (2009) 1684–1688.
- M. Mardani, R. Amrollahi, S. Koohestani, Design and construction of Alborz tokamak vacuum vessel system, *Fusion Engineering and Design* 87 (2012) 1616–1620.
- K. Chung, Y. An, B. Jung, H. Lee, C. Sung, Y. Na, T. Hahm, Y. Hwang, Design features and commissioning of the Versatile Experiment Spherical Torus (VEST) at Seoul National University, *Plasma Science and Technology* 15 (2013) 244.

- A. Mancini, J. Ayllon-Guerola, S. J. Doyle, M. Agredano-Torres, D. Lopez-Aires, J. Toledo-Garrido, E. Viezzer, M. Garcia-Muñoz, P. F. Buxton, K.-J. Chung, et al., Mechanical and electromagnetic design of the vacuum vessel of the SMART tokamak, *Fusion Engineering and Design* 171 (2021) 112542.
- F. Huang, X. Chen, H. Chen, S. Liu, Electromagnetic and mechanical analyses for the vacuum vessel of NCST, *Fusion Engineering and Design* 200 (2024) 114185.
- American Society of Mechanical Engineers, Boiler and Pressure Vessel Code, Section II—Materials, Part D: Properties, ASME, New York, NY, 2019.
- P. Santra, V. Bedakihale, T. Ranganath, Thermal structural analysis of SST-1 vacuum vessel and cryostat assembly using ANSYS, *Fusion engineering and design* 84 (2009) 1708–1712.
- Y. tao Song, D. Yao, S. Wu, P. Weng, Structural analysis and manufacture for the vacuum vessel of experimental advanced superconducting tokamak (EAST) device, *Fusion engineering and design* 81 (2006) 1117–1122.